

Mechanical signals at the base of a rat vibrissa: the effect of intrinsic vibrissa curvature and implications for tactile exploration

Brian W. Quist and Mitra J. Z. Hartmann

J Neurophysiol 107:2298-2312, 2012. First published 1 February 2012; doi:10.1152/jn.00372.2011

You might find this additional info useful...

Supplemental material for this article can be found at:

<http://jn.physiology.org/content/suppl/2012/02/02/jn.00372.2011.DC1.html>

This article cites 33 articles, 10 of which can be accessed free at:

<http://jn.physiology.org/content/107/9/2298.full.html#ref-list-1>

Updated information and services including high resolution figures, can be found at:

<http://jn.physiology.org/content/107/9/2298.full.html>

Additional material and information about *Journal of Neurophysiology* can be found at:

<http://www.the-aps.org/publications/jn>

This information is current as of May 2, 2012.

Mechanical signals at the base of a rat vibrissa: the effect of intrinsic vibrissa curvature and implications for tactile exploration

Brian W. Quist¹ and Mitra J. Z. Hartmann^{1,2}

¹Biomedical Engineering Department and ²Mechanical Engineering Department, Northwestern University, Evanston, Illinois

Submitted 25 April 2011; accepted in final form 26 January 2012

Quist BW, Hartmann MJZ. Mechanical signals at the base of a rat vibrissa: the effect of intrinsic vibrissa curvature and implications for tactile exploration. *J Neurophysiol* 107: 2298–2312, 2012. First published February 1, 2012; doi:10.1152/jn.00372.2011.—Rats actively tap and sweep their large mystacial vibrissae (whiskers) against objects to tactually explore their surroundings. When a vibrissa makes contact with an object, it bends, and this bending generates forces and bending moments at the vibrissa base. Researchers have only recently begun to quantify these mechanical variables. The present study quantifies the forces and bending moments at the vibrissa base with a quasi-static model of vibrissa deflection. The model was validated with experiments on real vibrissae. Initial simulations demonstrated that almost all vibrissa-object collisions during natural behavior will occur with the concave side of the vibrissa facing the object, and we therefore paid particular attention to the role of the vibrissa's intrinsic curvature in shaping the forces at the base. Both simulations and experiments showed that vibrissae with larger intrinsic curvatures will generate larger axial forces. Simulations also demonstrated that the range of forces and moments at the vibrissal base vary over approximately three orders of magnitude, depending on the location along the vibrissa at which object contact is made. Both simulations and experiments demonstrated that collisions in which the concave side of the vibrissa faces the object generate longer-duration contacts and larger net forces than collisions with the convex side. These results suggest that the orientation of the vibrissa's intrinsic curvature on the mystacial pad may increase forces during object contact and provide increased sensitivity to detailed surface features.

whisker; somatosensory system; trigeminal ganglion; active sensing; active touch; exploratory behavior

RATS ARE NOCTURNAL ANIMALS with low-acuity vision (Burn 2008). They use rhythmic (5–25 Hz) movements of their large mystacial vibrissae to tactually extract an object's spatial features (Berg and Kleinfeld 2003; Welker 1964). About 30 macrovibrissae are arranged in a regular array on each side of the rat's face (Brecht et al. 1997). The base of each vibrissa is embedded within a densely innervated follicle, where mechanoreceptors transduce deformations to electrical signals and provide input to primary sensory neurons in the trigeminal ganglion (Ebara et al. 2002).

Within nearly every brain structure of the vibrissal-trigeminal system, neurons are grouped to reflect the regular arrangement of vibrissae on the rat's mystacial pad (Arvidsson and Rice 1991; Ma and Woolsey 1984; Vanderloos 1976; Woolsey et al. 1975). The presence of these neural maps allows researchers to record from neurons responsive to particular groups of vibrissae, and has made the rat vibrissal system one

of the premier models to study how information is encoded and transformed along a primary afferent pathway.

Most neurophysiological studies to date have employed passive deflections of vibrissae, often trimming the vibrissa to a length of a few millimeters before applying controlled stimuli (e.g., Lichtenstein et al. 1990; Stuttgen et al. 2008). During natural exploration, however, rats typically make object contact much closer to the tip of the vibrissae (Grant et al. 2009; Mitchinson et al. 2007). Thus, under natural conditions, the deformations of the mechanoreceptors in the follicle will be strongly influenced by geometric features of the vibrissa, such as its taper and intrinsic curvature. In particular, the intrinsic curvature of the vibrissae has been shown to vary systematically across the array (Towal et al. 2011), and this will clearly have a strong effect on the mechanical signals sensed at the vibrissal base.

To date, the mechanical signals that will be present at the base of the vibrissae during active whisking behavior have not been quantified. The goal of the present work was to begin to quantify the forces and moments that a rodent will experience during active whisking, paying particular attention to the influence of intrinsic vibrissa curvature. Both simulations and experiments demonstrate that vibrissa-object collisions that occur with the vibrissa oriented concave forward will generate larger net forces than collisions at other orientations.

To ensure the direct, meaningful connection of these mechanical results to experimental observation of whisking behavior, we frame our RESULTS as answers to specific questions that may arise when observing a rodent whisking against objects. We also discuss how experimentalists can obtain approximations to the forces and moments described in this article by quantifying the shape of the vibrissa during active whisking behavior.

METHODS

Definitions of Variables

Intrinsic curvature of the vibrissa, A. Previous studies have shown that the proximal 60–70% of the vibrissa is approximately planar. As shown in Fig. 1A, the shape of a vibrissa can be well approximated by a parabola $y = Ax^2$, provided its base point is placed at the origin and the initial slope of the vibrissa is aligned with the x -axis (Knutson et al. 2008; Towal et al. 2011). Although this mathematical description is not coordinate invariant, it is an intuitive measure of vibrissa shape. An experimentalist could easily determine the quadratic coefficient A by measuring the resting shape of the vibrissa during a behavioral experiment, and that coefficient would then allow a unique identification of that particular vibrissa's geometry. Throughout this article, we therefore use the quadratic coefficient A as a unique measure of the vibrissa's intrinsic curvature.

Address for reprint requests and other correspondence: M. J. Z. Hartmann, Mechanical Engineering Dept., Northwestern Univ., 2145 Sheridan Rd., Evanston, IL 60208 (e-mail: m-hartmann@northwestern.edu).

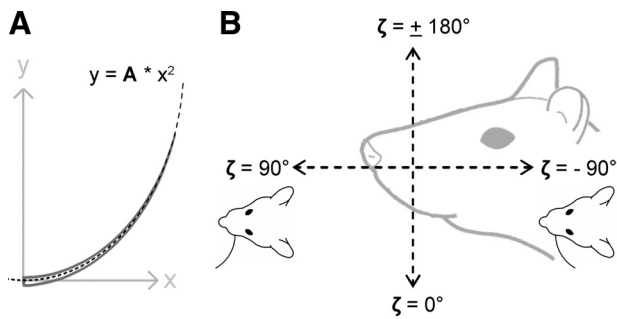


Fig. 1. Key variables used to describe vibrissa shape and orientation. *A*: the intrinsic curvature of the vibrissa (A) is approximately quadratic. *B*: the orientation of the intrinsic curvature of the vibrissa on the rat's mystacial pad is defined by the angle ζ .

Importantly, the coefficient A is not the curvature κ in the formal mathematical sense. For example, for the parabola $y = Ax^2$, the curvature κ is $\kappa = 2A/[1 + (2Ax)^2]^{3/2}$. The coefficient A is simply a convenient “handle” by which to describe the shape of a vibrissa. It is a single parameter uniquely related to, but not exactly, the curvature of the vibrissa.

It is important to note that as the vibrissa rotates against an object, it will change its curvature as it bends. We computed changes in curvature in the formal mathematical sense via numerical simulation, described later in METHODS.

Orientation of the vibrissa's intrinsic curvature, ζ . Because the vibrissae have an intrinsic curvature, a variable (ζ) is required to define how this curvature is oriented on the rat's mystacial pad (Knutsen et al. 2008; Towal et al. 2011). Figure 1*B* illustrates that the angle ζ is defined in a head-centered coordinate system with the horizontal axis parallel to the vibrissal rows. In this orientation, $\zeta = 0^\circ$ means that the vibrissa's curvature points concave ventral. $\zeta = \pm 180^\circ$ means the vibrissa's curvature points concave dorsal. $\zeta = +90^\circ$ means the vibrissa's curvature points concave rostral. $\zeta = -90^\circ$ means the vibrissa's curvature points concave caudal.

Vibrissa-object collisions fall on a continuum, from perfectly concave forward to perfectly concave backward. As shown in Fig. 2*A*, three planes are required to describe a three-dimensional (3D) collision of a vibrissa with an object: first, the plane of the intrinsic curvature of the vibrissa, defined by the angle ζ (cf. Fig. 1*B*); second, the plane of rotation of the vibrissa, defined by the axis about which the vibrissa rotates; and third, the plane of the object surface, defined as the plane tangent to the object surface at the point of vibrissa contact. The relative angles between these three planes dictate the mechanics of the vibrissa-object interaction.

Figure 2*B* illustrates that there exists a continuum of vibrissa collision types determined by the relationship between the plane of rotation and the plane of the vibrissa. Collisions can be broadly categorized into either concave forward (CF) or concave backward (CB), indicating the direction of the concave side of the vibrissa with respect to the object during a collision. The extremes of this continuum occur when the vibrissa curvature exists entirely within the plane of rotation, and are referred to as perfectly CF and perfectly CB. In the example of Fig. 2*B* the plane of rotation is illustrated as the horizontal plane, and therefore perfectly CB or CF collisions occur in the horizontal plane. If one imagines rotating the entire figure, it is clear that the plane of rotation can be any plane, and perfectly CF and perfectly CB collisions can therefore occur in any plane.

It is clear from Fig. 2 that a full 3D simulation is required to model the mechanics of the most general vibrissa-object collision. During natural behavior the intrinsic curvature of the vibrissa does not generally lie in the plane of rotation. In addition, depending on how the object is oriented, the vibrissa can slip on the object out of the plane of rotation. To quantify the complete mechanical signal at the

vibrissa base would therefore require three reaction forces and three reaction moments.

As a simplification, the present study focused on the extremes of the collision continuum: perfectly CF and CB collisions. All loading and bending is assumed to occur within the plane of rotation. This effectively reduces mechanics to two dimensions, leaving two reaction forces and one reaction moment to be computed (described later in METHODS).

It is important to note that the results of this study apply to most collisions, but subject to important constraints. Specifically, the mechanics of a collision that falls between perfectly CF and perfectly CB can be modeled by projecting the vibrissa curvature (A) into the plane

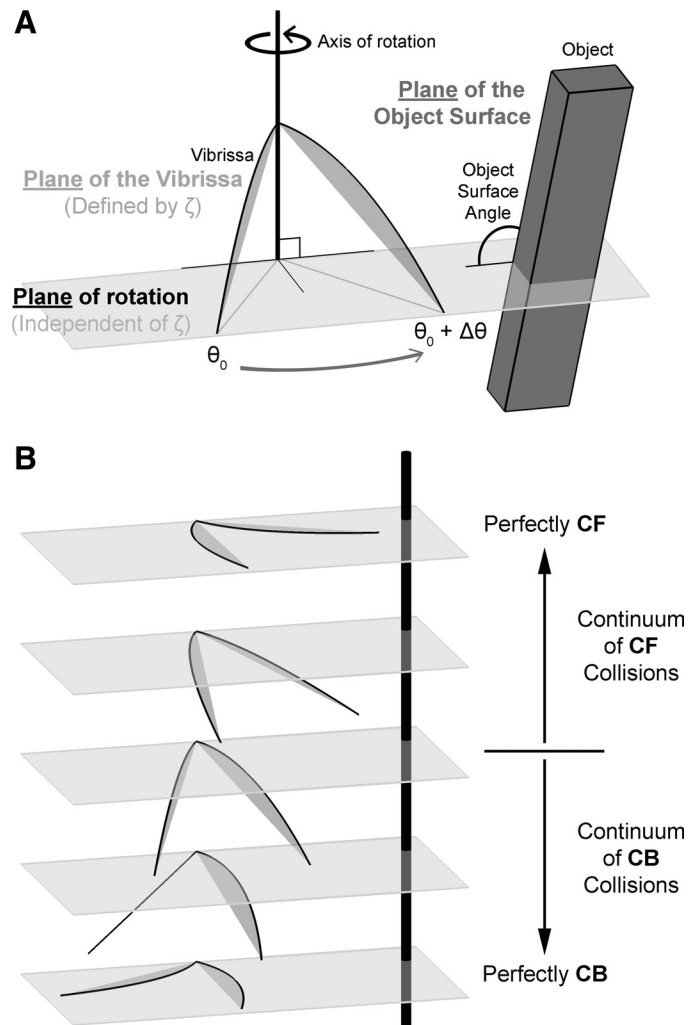


Fig. 2. Key variables used to describe 3-dimensional (3D) vibrissa collisions. *A*: in a 3D collision, there are 3 relevant planes: the plane of the intrinsic curvature of the vibrissa, the plane of rotation, and the plane of the object surface. The plane of the vibrissa is defined by the angle ζ . The plane of rotation is defined as the plane normal to the axis about which the vibrissa rotates. This plane is independent of the angle ζ . Finally, the plane of the object surface is defined as the plane tangent to the object surface at the point of vibrissa contact. The relative angles between the 3 planes dictate how the vibrissa will interact with the object. For the purposes of this study, the plane of the object surface is always perpendicular to the plane of rotation. *B*: there exists a continuum of vibrissa collision types, categorized broadly as occurring against either the concave forward (CF) or the concave backward (CB) face of the vibrissa. A perfectly CF/CB collision occurs when the intrinsic curvature of the vibrissa remains in the plane of rotation. This study focuses specifically on the 2 extremes of the collision spectrum: perfectly CF and perfectly CB collisions. Note that in this particular figure the plane of rotation happens to be the horizontal plane, but in principle it can be any plane.

of rotation and then appropriately calculating forces and moments at the vibrissal base. Guidelines for how to apply the results of the present study to real behavioral data are provided in DISCUSSION.

Arc length of vibrissa-object contact, s , and angle of rotation against the object, theta push θ_p . In the present study, we consider only collisions between the vibrissa and a point object. We can therefore precisely define the location along the vibrissa arc length (s) at which object contact occurs. Figure 3A illustrates that this contact location can be represented as a fraction of the total vibrissa arc length.

The angle that describes how far the vibrissa has rotated against the object is defined by the variable theta push (θ_p) (Fig. 3A). θ_p is defined to equal 0° at the angle at which the vibrissa first makes contact with the object.

Forces and moment at the base of the vibrissa: “axial force” F_x , “transverse force” F_y , and moment M_z . As a vibrissa rotates into the object ($\theta_p > 0^\circ$), reaction forces and moments will develop at the base. These are the mechanical signals that will be transmitted to the mechanoreceptors within the follicle. By assuming that all bending occurs in the plane of rotation, the problem reduces to a single moment (M_z) and two forces (F_x and F_y) at the vibrissa base, illustrated in Fig. 3B.

By convention, forces along the long axis of the vibrissa, F_x , are referred to as axial forces (Hibbeler 2011). Compressive loading of the vibrissa generates a negative axial force, while tensile loading generates a positive axial force (Hibbeler 2011). Conceptually, it may be easiest to think of the sign of the axial force with respect to the follicle. A force vector pointing in the positive x -direction means the vibrissa is being “pulled out” of the follicle. A force vector pointing the negative x -direction means the vibrissa is being “pushed into” the follicle.

Also by convention, forces acting in the y -direction, F_y , are referred to as transverse forces (Hibbeler 2011). Positive transverse forces point in the positive y -direction, and negative transverse forces point in the negative y -direction.

Figure 3B illustrates that forces and moments are defined with a right-hand coordinate system aligned with the long axis of the vibrissa base (Birdwell et al. 2007; Solomon and Hartmann 2006, 2008, 2010). The local vibrissa-centered coordinate frame moves with the vibrissa, and therefore rotates along with θ_p . This ensures that the axial force always corresponds to the force component directed axially, parallel to the vibrissa as it emerges from the follicle.

Any force acting at a distance away from the follicle will generate a bending moment at the base of the vibrissa. The moment at the vibrissa base resists the rotation caused by the applied force. Moment is equal to the cross product between the vector that connects the vibrissa base to the point of object contact and the force vector.

Moment M_z is defined positive for a counterclockwise rotation. In our simulations and experiments, all forces were applied in the negative y -direction, so M_z is always negative (Fig. 3B).

Simulation: Numerical Model of Vibrissa Bending, Moment, and Forces

To simulate vibrissa bending we used the numerical simulation method of Solomon and Hartmann (2006), also used by Birdwell et al. (2007). This model is quasi-static. It also assumes that the total applied force always acts normal to the vibrissa, which means there is assumed to be no friction.

The axial force and transverse force at the vibrissa base were computed in two steps. First, the total force at the base was set equal to the total applied force. The total force was then divided into axial and transverse components based on the geometry of the vibrissa.

The simulation works by computing the vibrissa’s local curvature at the location of the applied force and then computing changes in local curvature back to the vibrissa base. To begin, the vibrissa is discretized into a series of rigid links connected by torsional springs. At each node i , the change in curvature, κ_i , is related to the moment, M_i , by the equation

$$\kappa_i = \frac{M_i}{E_i I_i} \quad (1)$$

where E_i is Young’s modulus and I_i is the area moment of inertia of the node i .

At the start of the simulation, Young’s modulus and the area moment of inertia are set for each node (Quist et al. 2011). The user provides the location in (x, y) coordinates of the point object relative to the vibrissa base. This location is denoted as (a, b) . The algorithm then searches for a stable configuration of the vibrissa by varying two parameters: the force applied and the arc length (s_x, s_y) at which the force acts. Changes in curvature are computed for each node with Eq. 1, and the MATLAB function `fminsearch` is used to vary the applied force and the location of (s_x, s_y) to minimize the Euclidean distance between the points (a, b) and (s_x, s_y) .

Unless otherwise stated, simulations used parameters typical of a C2 vibrissa. Vibrissa length was set to 35 mm (Towal et al. 2011); taper ratio (base diameter divided by tip diameter) was set to 15 (Williams and Kramer 2010); elastic modulus was set to 3 GPa (Birdwell et al. 2007; Hartmann et al. 2003; Quist et al. 2011; Solomon and Hartmann 2006); and base diameter was measured from a similar-sized vibrissa to be $163 \mu\text{m}$. As described in *Definitions of Variables*, we took the quadratic coefficient A as a measure of intrinsic curvature. For a typical C2 vibrissa, A is 0.0233 (Towal et al. 2011), and this was the value used to generate the data shown in Figs. 8 through 10.

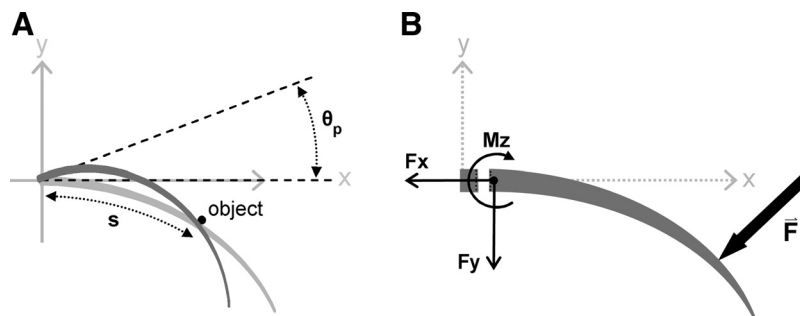


Fig. 3. Key variables used to describe vibrissa mechanics. *A*: schematic of a vibrissa rotating against a point object. The arc length at which the vibrissa makes contact with the object, s , is represented as a fraction of the total arc length of the vibrissa. Rotations of the vibrissa against the object in the plane of rotation (in this example, the x - y plane) are indicated with theta push (θ_p). θ_p equals 0° at the angle at which the vibrissa first makes contact with the object. *B*: in the most general case, there will be 3 reaction forces and 3 reaction moments at the base of the vibrissa resulting from an applied force. If we assume that the intrinsic curvature of the vibrissa always lies in the plane of rotation, then this reduces to 2 reaction forces (axial force F_x and transverse force F_y) and 1 reaction moment (M_z) at the base. All variables are negative in the directions shown.

The C2 vibrissa was selected for two reasons. First, using the data of Towal et al. (2011), we determined that the coefficient A for a column 2 vibrissa is closest to the median A coefficient across all vibrissae. Second, the C row is close to the center of the array. Thus the C2 vibrissa is representative of a “typical” vibrissa.

We also performed a set of simulations to determine the effect of varying the vibrissa’s intrinsic curvature (see Fig. 11). In these simulations the A coefficient was varied from -0.1 to $+0.1$ in increments of 0.005 . This range encompasses the complete physiological range for curvatures reported by Towal et al. (2011).

It is important to note that the simulation results presented here provide estimates on the magnitudes of the forces and moments that any given vibrissa would produce. Natural variability in actual vibrissa parameters will cause the actual forces and bending moment to vary. This variation will only affect the magnitudes of the forces and bending moment. For example, if the elastic modulus were 10% larger, then the forces and bending moment would also be 10% larger.

Experiment: Measurement of Two Components of Force During the Sweep of a Vibrissa Past a Point Object

All procedures were approved in advance by Northwestern University’s Animal Care and Use Committee. Vibrissae were plucked from five female Sprague-Dawley rats that had been anesthetized in unrelated experiments. Rats were ~ 3 mo old and weighed ~ 300 g. Only a single vibrissa was plucked from each rat. A total of five vibrissae across the array were selected to provide a sample of the macrovibrissae. The specific vibrissae selected were A1, A3, C3, E1, and E3. All experiments were completed within 36 h of plucking.

The experiment is conceptually summarized in Fig. 4A. We measured the forces generated as a vibrissa was rotated into a sensitive two-dimensional (2D) force sensor (Quist and Hartmann 2008). The sensor was held in a micromanipulator and placed at seven different radial distances along the length of the vibrissa. The vibrissa was then rotated either clockwise or counterclockwise to generate either a CF or a CB collision with the sensor. The full experimental setup included the 2D force sensor, a precision-actuated micromanipulator, and a DC motor, each of which is described in more detail below.

A detailed description of the sensor’s construction and characterization can be found in Quist and Hartmann (2008). Briefly, two orthogonally mounted pairs of strain gauges (SG-3/350-LY11, Omega Engineering) were used to measure the deflection of a 0.025-in.-diameter nitinol wire (NW-025, Small Parts). The output from each pair of strain gauges formed one-half of a Wheatstone half-bridge, and the resulting signal was amplified with an instrumentation amplifier. The voltage output from the sensor was low-pass filtered in hardware at $\sim 1,500$ Hz and sampled at 3 kHz by a NI-DAQ board (NI-6059, National Instruments). The voltage output from each sensor axis (i.e., each strain gauge pair) was calibrated gravimetrically by hanging a series of small graduated weights near the sensor tip. The linear output was fit with a least-squares regression, and the resulting equation was

used to calibrate the sensor output (in volts) to the force acting on the sensor (in millinewtons). This calibration is valid only when the forces act at the same distance along the sensor’s length as the calibration weights. We ensured that this condition held when collecting all data for this experiment.

The sensor was clamped to a precision-actuated micromanipulator (MP-285, Sutter Instrument) with a custom-machined attachment. The micromanipulator had $0.2\text{-}\mu\text{m}$ resolution in three orthogonal directions and could be controlled through a LabVIEW interface. The two axes of the sensor were aligned with two of the micromanipulator axes, and the remaining axis of the micromanipulator was used to position the sensor vertically. This alignment ensured a consistent relationship between the voltage output of each channel and force direction.

The base of each vibrissa was rigidly fixed with superglue (Loctite Super Glue, Henkel) to a stage directly connected to the shaft of a DC motor. The vibrissa was carefully positioned with respect to the center of rotation under a dissection microscope to ensure that 1) the intrinsic curvature of the vibrissa was in the plane; 2) the vibrissa base was axis-aligned with one of the axes of the sensor; and 3) only the proximal ~ 1 mm of the vibrissa base was glued to the stage, corresponding to the bulb that inserts into the follicle. The motor was equipped with an optical encoder (A-Max 32, Maxon Motors) with 2,000 counts per revolution ($0.18^\circ/\text{step}$). The motor was controlled with an EPOS 24/1 controller (Maxon Motors) via a LabVIEW interface. The digital output from the motor encoder was also sampled by the NI-DAQ board at 3 kHz.

Seven radial distances of the sensor and two orientations of the vibrissa’s curvature toward the sensor were tested. The arc lengths were 25%, 50%, 75%, 80%, 85%, 90%, and 95% of the total vibrissa length. Some longer vibrissae were not tested at their more distal arc lengths because the micromanipulator had a limited range of travel. The two curvature orientations tested were impacts between the vibrissa’s CF face and the vibrissa’s CB face with the force sensor (see Fig. 4B).

For each mechanical test of the vibrissa, the sensor was moved to a selected radial distance and the motor then rotated to sweep the vibrissa all the way past the sensor. The velocity of the motor was constant, and slow enough to avoid dynamic effects (3 revolutions/min). Each sweep was performed 25 times for both curvature orientations at each radial position of the sensor. The CF side of the vibrissa collided with the sensor if the motor was run in one direction (e.g., clockwise), and the CB side of the vibrissa collided with the sensor if the motor was run in the opposite direction (e.g., counterclockwise). Under our tightly controlled conditions, the vibrissa made contact with the sensor perpendicular to its plane of rotation and did not slip along the sensor’s length.

In postprocessing within MATLAB, voltage changes in the two sensor axes were converted to forces and then low-pass filtered at 80 Hz. Motor encoder angle was linearly interpolated between the 0.18° steps. For each trial, the angle at which the vibrissa first contacted the

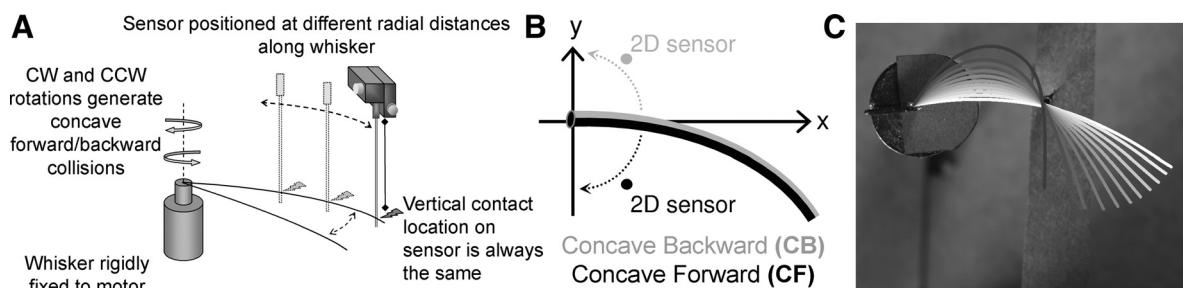


Fig. 4. Experimental setup and images of vibrissa deflections. **A**: schematic of experimental setup. A vibrissa is mounted to a motor and rotated against a custom-built force sensor, positioned with a micromanipulator. CW, clockwise; CCW, counterclockwise. **B**: the vibrissa was rotated so that either its CF or its CB face collided with the object. 2D, 2-dimensional. **C**: the full shape of the vibrissa was tracked as it was rotated against a peg. Color changes from white to black as the vibrissa is rotated through an increasing angle against the peg. Images are separated by 5° of rotation.

sensor was set to 0° . The measured forces from the sensor (fixed, global coordinates) were then transformed via a rotation to the forces that would occur at the vibrissa base (local coordinates centered on the axis of motor rotation). For each rotation angle, bending moment was computed as the cross product of the distance vector from the vibrissa base to the point of vibrissa-sensor contact and the force vector obtained from sensor readings.

Fitting Model to Experiment

To match experimental and simulation results, we needed to measure the diameter of the vibrissa at its base as well as the 2D undeflected shape of the vibrissa. The diameter at the vibrissa base, along with the vibrissa's taper ratio, defines the area moment of inertia, $I = \pi d^4/64$, at each location along the vibrissa. The undeflected shape of the vibrissa is needed to decompose forces into axial and transverse components. An example of the undeflected shape of the vibrissa is shown as the white trace in Fig. 4C.

The diameter of the vibrissa base was measured from a microscope image of the proximal ~ 1 cm of the vibrissa. Images were acquired with a standard bright field microscope with a $\times 4$ objective and a camera attachment. All images were processed in MATLAB. Determination of the base diameter was straightforward given the resolution of the system ($1.34 \mu\text{m}/\text{pixel}$) and high contrast of the bright field image. Each image was converted to black and white with a threshold and placed in a standard Cartesian coordinate frame. The upper and lower boundaries of the vibrissa were then extracted. These boundaries varied within the image by approximately $\pm 10 \mu\text{m}$. The diameter of the vibrissa base was then calculated as the median of the upper image boundary minus the median of the lower image boundary.

In some experiments, we used a 6.3-megapixel camera (Canon EOS 300D Digital Rebel) to obtain top-down ("bird's eye") images of the shape of the vibrissa as it was rotated against a point object. In these experiments, a rigid peg replaced the sensor in Fig. 4A. The shape of the vibrissa was imaged as it rotated in increments of 5° past the peg. Images were processed in MATLAB to extract vibrissa shape. Each image was converted to black and white and the vibrissa shape determined in (x, y) coordinates and scaled from pixels to millimeters. Example output is shown in Fig. 4C. These experimental measurements of vibrissa shape were then compared with the vibrissa shape predicted from simulation.

The forces predicted by the model were fit to the forces determined experimentally by varying the elastic modulus, E . Starting with the 2D shape of the undeflected vibrissa, we used the model to predict deflection-force curves assuming an initial value for E of 1 GPa. This value of E was then varied with a gradient decent algorithm that minimized the absolute value of the difference in total force magnitude between model and experiment. The total force magnitude was the vector sum of the axial and transverse forces at the point of object contact. This procedure was performed for each radial distance and rotation direction. Best values for E ranged between 3.7 and 4.9 GPa, well within previously published ranges (Birdwell et al. 2007; Hartmann et al. 2003; Quist et al. 2011; Solomon and Hartmann 2006).

RESULTS

RESULTS is divided into three main sections. The first section quantifies the orientation of the vibrissae during natural whisking behavior and demonstrates that most protractions will result in CF collisions. The second section presents simulations that quantify the effect of intrinsic curvature on the mechanical signals that will be transduced by mechanoreceptors in the follicle. The final section contains experimental results that validate the simulation and answer questions that simulations cannot address.

To ensure the direct, meaningful connection of these mechanical results to experimental observation of whisking be-

havior, each subsection is framed as an answer to a specific question that may arise when observing a rat whisking against objects. Some suggestions for how to apply these results to the quantification of whisking behavior are provided in DISCUSSION.

Intrinsic Vibrissa Curvature During Natural Whisking Behavior

What is the orientation of intrinsic vibrissa curvature during natural behavior? The schematic in Fig. 5 provides an intuition for why the intrinsic curvature of the vibrissa is important. A force applied to a vibrissa with large intrinsic curvature (Fig. 5A) will generate different reaction forces F_x and F_y than the same force applied to a vibrissa with small intrinsic curvature (Fig. 5B). These forces will directly affect the deformation of mechanoreceptors within the follicle.

As described in METHODS, the shape of a vibrissa can be characterized as a parabola of the form $y = Ax^2$ (Knutsen et al. 2008; Towal et al. 2011). The coefficient A is a unique "handle" to the curvature of the vibrissa that is relatively easy to measure during behavioral experiments. We first characterized the distribution of the magnitudes of intrinsic curvature across vibrissae and then quantified the orientation of intrinsic curvature across the array.

Figure 6A uses data from Towal et al. (2011) to quantify the coefficient A as a function of vibrissa length for 354 vibrissae from 6 rats. On average, shorter vibrissae have a larger intrinsic curvature than longer vibrissae. Because rostral vibrissae tend to be shorter than caudal vibrissae, they tend to have greater intrinsic curvature (Towal et al. 2011). At present, it is not known why shorter vibrissae have greater curvature. In addition, the variability in intrinsic curvature is much larger for shorter vibrissae than for longer vibrissae. Finally, there is a remarkably distinct "upper bound" on the maximum curvature of the vibrissa. This upper bound was well fit by the equation $y = 0.156e^{(-x/15.6)} + 0.015$.

Figure 6B quantifies the distribution of curvatures across vibrissae using the data set from Fig. 6A. Ninety percent of vibrissae have intrinsic curvatures between 0.0065/mm and 0.074/mm.

So far, we have discussed the magnitude of a vibrissa's intrinsic curvature, as quantified by the coefficient A . This magnitude is different from the orientation of the vibrissa's curvature on the rat's mystacial pad.

The orientation of a vibrissa's curvature on the mystacial pad is defined by the angle ζ (Knutsen et al. 2008; Towal et al. 2011). Towal et al. (2011) quantified ζ for all vibrissae across

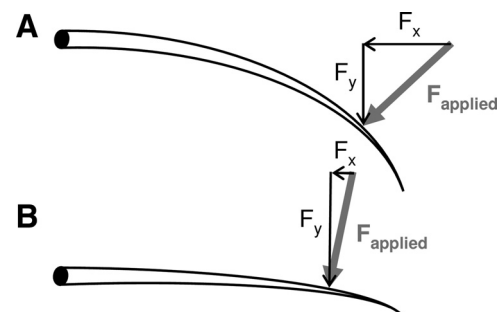


Fig. 5. A force applied to a vibrissa will generate different reaction forces F_x and F_y depending on the intrinsic curvature of the vibrissa. *A*: a vibrissa with a large intrinsic curvature (large value of A). *B*: a vibrissa with a small intrinsic curvature (small value of A).

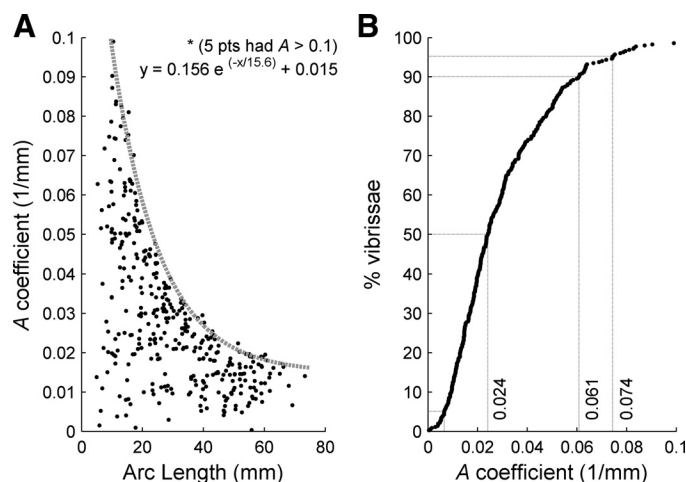


Fig. 6. Intrinsic curvature of the vibrissae varies across the array. *A*: the coefficient A , a measure of intrinsic curvature, decreases with vibrissal arc length. On average, shorter vibrissae have larger intrinsic curvature. *B*: fraction of vibrissae (of 354 total) with given intrinsic curvatures. Line at 5% of vibrissae corresponds to an A coefficient of 0.0065/mm. Data are from Towal et al. (2011).

the array with the animal at rest, and Knutsen et al. (2008) established a set of equations relating changes in ζ to the protraction angle θ during active whisking. Together, these studies allow us to determine how the distribution of curvatures across the array will change during a whisk. A movie of the simulated protraction can be found in Supplemental Video S1.¹

The orientation of the intrinsic curvature of the vibrissae at rest and after a protraction of 40° is shown in Fig. 7. Starting with the vibrissae in their resting orientation, we used equations that relate ζ and protraction angle θ (Knutsen et al. 2008) to simulate how ζ will change during a protraction of the vibrissae through 40° in θ . The unit normal vectors shown inside each circle of Fig. 7 represent ζ , and thus define the direction in which the vibrissa would have to rotate in order to experience a perfectly-CF collision (cf. Fig. 2*B*). The short bars near the bottom of Fig. 7 represent the location and orientation of an object surface that would be exactly perpendicular to the vibrissae during the perfectly CF collision.

Figure 7 provides three insights into the orientation of vibrissae during a whisk. First, the rotation of each vibrissa about its own axis (i.e., the “roll” of each vibrissa as defined by Knutsen et al. 2008) does not have a large effect on ζ . The pre- and postprotraction orientation vectors overlap considerably. Second, all but five vibrissae are oriented so that ζ lies between 0° (concave ventral) and $+90^\circ$ (concave rostral). This means that all but these five vibrissae will experience a CF collision for a vertical surface placed in front of the rat. Third, the array may be seen to be divided into two regions, with column three serving as an approximate dividing line. Vibrissae rostral to column three are likely to undergo near-perfect CF collisions during a standard rostral-to-caudal whisking movement. In contrast, vibrissae caudal to column three are oriented more concave down. This means that they will essentially interact with an object placed vertically in front of the rat as though they had no intrinsic curvature ($A = 0$). However, they will experience near-perfect CF collisions for small angles of rota-

tion for any object surface beneath the rat (e.g., the ground). This type of collision would likely occur as the rat makes “head-dabbing” movements during navigation behavior.

Summarizing, Fig. 7 reveals that for small angles of rotation vibrissae will experience near-perfect CF collisions for tapping on object surfaces that essentially mirror the shape of the rat’s snout. In light of this feature of vibrissal array geometry, we sought to understand why the morphology of the array is so heavily weighted toward CF collisions. What effect does curvature have on the mechanical signals that will be generated, and what advantages might CF collisions confer over CB collisions?

Simulation Results

How do forces at the vibrissa base depend on intrinsic vibrissa curvature? We begin with an example that provides an intuition for the role of intrinsic vibrissal curvature in the mechanics of object contact. It is important to understand, from the onset, that there is a unique, one-to-one relation between the deflected shape of the vibrissa and the forces that will be generated at the base.

Using numerical simulations, we modeled the deflection of a typical C2 vibrissa rotating against a peg placed at 50% along its arc length. We simulated both CF and CB collisions of the vibrissa as it rotated a total of 30° against the peg. Each of the small subplots of Fig. 8 illustrates the shape of the vibrissa at different values of θ_p . The components of force (axial and transverse) associated with each of these deflections are depicted in the central plot.

It is immediately clear that collisions with different curvatures result in different force trajectories at the vibrissa base. A CB collision generates force components that are initially equal but then develops larger axial forces. A CF collision initially generates very small axial forces and develops large transverse forces.

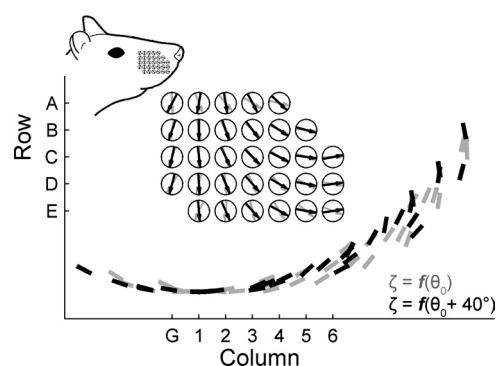


Fig. 7. Orientations of the vibrissae on the rat’s face define the directions that each vibrissa would have to rotate to experience a perfectly CF collision. The base points of each vibrissae are represented by the large circles. The arrows in each of the circles are unit-normals that lie in the plane of intrinsic vibrissa curvature and are perpendicular to the vibrissa at its base as it emerges from the mystacial pad. Arrows indicate the CF direction of the vibrissa’s intrinsic curvature. Orientations are shown for the vibrissal array at rest (gray) and after a simulated protraction of 40° (black). For each vibrissa, a short bar near *bottom* indicates the orientation of a surface normal to the plane of vibrissa curvature. The radial distance from the vibrissa to the short bar is arbitrary and selected to be approximately equidistant from the center of the array. Surface orientations are again shown for the vibrissal array at rest (gray) and after a simulated protraction of 40° (black). *Inset*: approximate orientation of the vibrissal array on the rat’s mystacial pad.

¹ Supplemental Material for this article is available online at the Journal website.

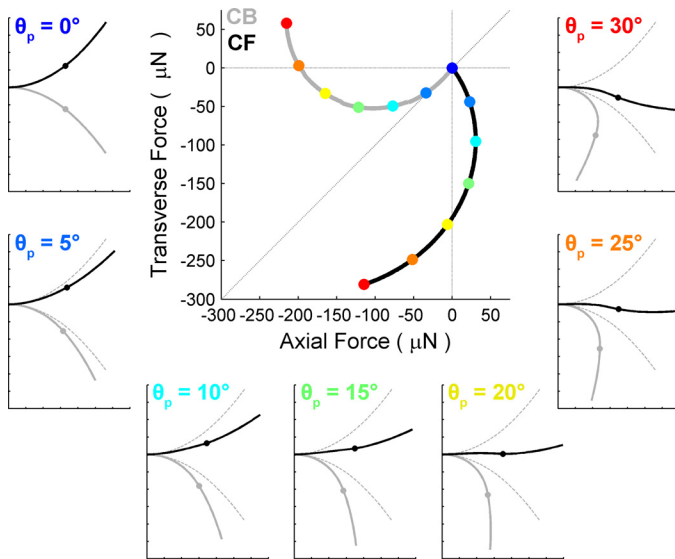


Fig. 8. Simulations of CF (black) and CB (gray) rotations of the vibrissa against a point object. Each of the small subplots illustrates the shape of the vibrissa at specific values of θ_p (5° increments). The shape of the deflected vibrissa is in the vibrissa coordinate frame; therefore, force components at the vibrissa base are aligned with the coordinate axes of the plot. Dotted lines indicate the shape and orientation that the vibrissa would have had, had it rotated through θ_p but not collided with an object. In each of the small subplots, the value of θ_p is assigned a color. Corresponding colored circles in the central plot indicate the force components at that value of θ_p .

Examination of the shape of the deflected vibrissae provides an intuition for these components of force. In the CB collision, the vibrissa begins developing axial forces immediately. At $\theta_p = 25^\circ$, almost the entire force vector is made up of axial forces. This is because the vibrissa is compressing in on itself. In contrast, a CF collision straightens out the vibrissa. At $\theta_p = 20^\circ$, the force vector is almost entirely made up of transverse forces.

What are the forces and moments that will be generated at the vibrissa base as the rat rotates its vibrissa past an object? Numerical simulations were used to model the forces and bending moment that would be generated as the rat rotated a vibrissa against a point object at different radial distances. We simulated a vibrissa with length, taper, and curvature typical of the C2 vibrissa and compared the results to those from a vibrissa of the same length and taper ratio but with zero intrinsic curvature (i.e., the vibrissa is straight).

Results of these simulations are shown in Fig. 9. In all subplots, the x -axis is the angle through which the base of the vibrissa has rotated after having made contact with the object, that is, the push angle, θ_p . From top to bottom, the rows of Fig. 9 illustrate the bending moment M_z , the transverse force F_y , and the axial force F_x at the vibrissa base as the vibrissa is rotated through an increasing push angle against a point object. From left to right, the radial distance of the point object is moved from 5% along the vibrissa length to 90% along the vibrissa length. Each subplot illustrates results for three vibrissae: a straight vibrissa (ST), a vibrissa with intrinsic curvature rotated to collide with its CF side into the object, and a vibrissa with the same intrinsic curvature rotated to collide with its CB side into the object.

Two clear trends emerge from these simulations. First, the magnitudes of moment and force components fall off sharply as the radial distance of the object increases. This is apparent in the reduced scale of the y -axis as radial distance s increases along each row of Fig. 9. Second, intrinsic vibrissa curvature has little effect on moments but a strong effect on forces. This effect becomes more pronounced as the object moves farther from the vibrissa base. Furthermore, the effects are strongest on the axial force F_x , as seen in the highly disparate traces associated with CF and CB collisions in the bottom row of Fig. 9. CB impacts generate axial forces that become increasingly negative until the vibrissa loses contact with the object. In

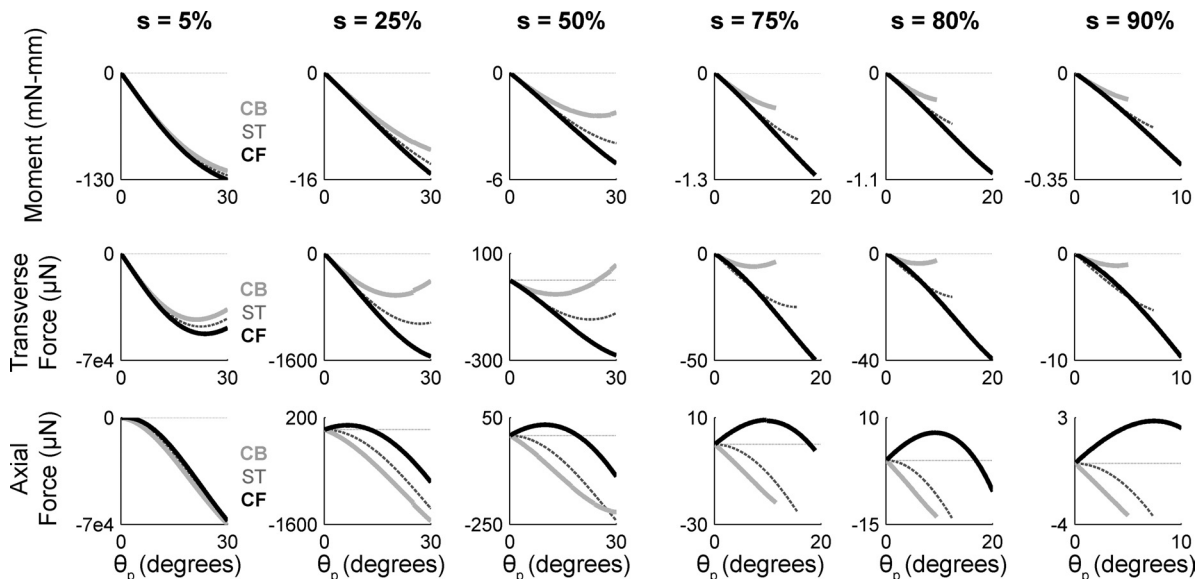


Fig. 9. Bending moment and forces as a vibrissa is simulated to rotate against a point object placed at different radial distances from the vibrissa base. Angle of rotation into the object is the pushing angle θ_p . Radial object distance s is indicated as % of vibrissa arc length at *top*. In all subplots, black traces represent results for a vibrissa with intrinsic curvature undergoing a CF collision, dark gray dashed traces represent results for a straight vibrissa (ST), and light gray traces represent results for a vibrissa with intrinsic curvature undergoing a CB collision. Force and moment traces in all plots stop at the angle at which the simulation became numerically unstable. *Top*: bending moment (M_z) at the vibrissa base. For all radial distances and all vibrissa curvatures, the magnitude of M_z increases monotonically with rotation angle until contact with the object is lost. *Middle*: transverse force F_y at the vibrissa base. *Bottom*: axial force F_x at the vibrissa base.

contrast, CF impacts generate axial forces that initially trend positive but then change direction and become increasingly negative until contact with the object is lost.

Intriguingly, we found that the angle at which F_x changes direction during a CF impact as well as the angle at which F_x changes sign are both uniquely related to radial object distance during concave impacts. This relationship holds up until $s \approx 75\%$ of the vibrissa length.

Supplemental Videos S2–S7 show simulations of the forces and bending moments that will be generated at the vibrissal base as the rat rotates its vibrissa past an object, and how these signals depend on intrinsic vibrissa curvature. The top rows of the videos illustrate the changes in vibrissal shape that will occur during ST, CF, and CB collisions, while the bottom rows illustrate the associated increases in bending moment, transverse force, and axial force. The numerical data generated by the simulations are provided as MATLAB files in Supplemental Data S1. The MATLAB function written to generate the numerical simulations is provided in Supplementary Text S1.

What is the range of forces and moments possible at the vibrissa base as the rat rotates the vibrissa against an object at different distances? The results of Fig. 9 can be replotted in a manner that more clearly reveals the range of forces and moments that will be present at the vibrissa base if the rat makes contact with an object at different locations along the vibrissa.

Imagine, for example, that the rat gently taps its vibrissae against an object through an angle of 1° . For simplicity, let the vibrissa be straight. Plotting the resulting M , F_y , and F_x (at a value of $\theta_p = 1^\circ$) as functions of radial distance (Fig. 10, A–C, thin black line) reveals that forces and moments vary over approximately three orders of magnitude.

Now, imagine that the rat pushes its vibrissae hard against an object through 10° of rotation at the base. Plotting the resulting M , F_y , and F_x (now at a value of $\theta_p = 10^\circ$) as functions of radial distance (Fig. 10, A–C, thick black line) reveals a range similar to that for the gentle tap, approximately three orders of magnitude. However, the absolute values of this range have increased in magnitude, making the “push” sensitivity appear as a DC-shifted version of the “tap” sensitivity curve.

Although these results were generated with simulations that assume a straight vibrissa, results were similar for a vibrissa with either curvature orientation (data not shown). Results are also similar for much smaller or larger vibrissae: the range of forces and moments present in the follicle for a given value of

θ_p was consistently found to vary over approximately two to three orders of magnitude for all vibrissae.

How does intrinsic vibrissa curvature affect forces and moment, and how does this effect vary if the object is located at different radial distances? An important trend illustrated by Fig. 9 is that intrinsic vibrissa curvature has little effect on forces if the object is close to the vibrissa base but a strong effect if the object is closer to the vibrissa tip. There is little effect of curvature for contacts with an object near the vibrissa base because all vibrissae (CF, ST, CB) are very similar in shape near the base. As the contact point moves farther out along the vibrissa length, the shapes of the vibrissae are increasingly disparate and the effects of curvature become more pronounced.

To examine these effects in detail, we varied the vibrissa's intrinsic curvature in simulations that modeled the vibrissa rotating against a peg placed at three radial distances. Results are shown in Fig. 11. Curvatures were varied to include all physiologically realistic curvatures, from quadratic coefficient $A = 0.1$ (an extremely curved rostral vibrissa) to $A = 0$ (perfectly straight). Negative and positive values of A indicate CB and CF collisions, respectively.

The top row of Fig. 11 illustrates that, as expected, the effect of curvature on bending moment is minimal, especially for small angles of rotation against the point object. As the vibrissa is increasingly rotated against the object, curvature begins to influence moment at the base. In particular, for a CB collision, the moment traces grow closer together as θ_p increases. This indicates that moment increases more gradually for CB collisions than for CF collisions. Intuitively, this result occurs because the CB orientation of the curvature causes the vibrissa to bend in on itself during the collision. In contrast, the CF orientation of the curvature causes the vibrissa to straighten out (cf. Fig. 8). When the vibrissa straightens, more of the force is oriented perpendicular to the moment-arm vector (a vector going from the vibrissa base to the point of object contact). Because the force vector and the moment-arm vector are more perpendicular, the CF collision generates larger bending moments than a CB collision for the same value of θ_p .

A similar, but more pronounced effect is observed for the transverse forces (Fig. 11, middle row). Transverse forces are very close to zero for CB collisions because the vibrissa is bending in on itself.

The effects of curvature on the axial force are even more striking, as shown in the bottom row of Fig. 11. As the

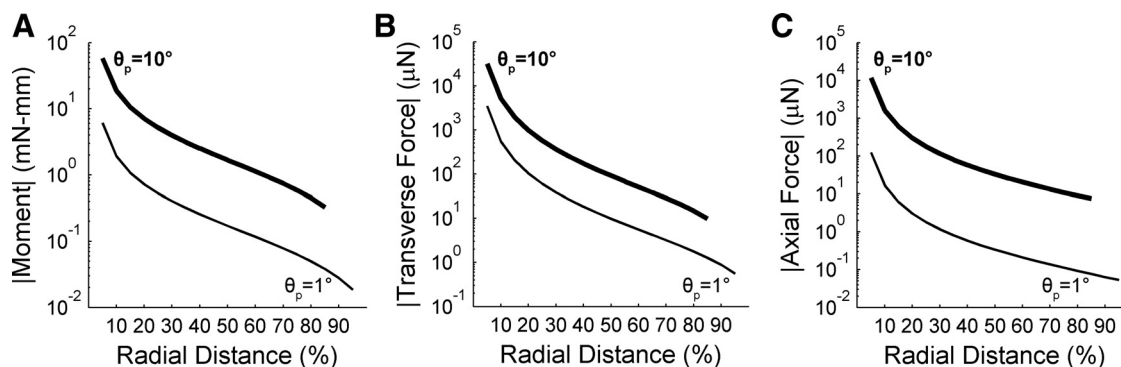


Fig. 10. Range of forces and moments that will be present at the base of the vibrissa during object contact: change in the magnitudes of moment and forces at the vibrissa as a function of radial distance and θ_p . For all plots, the thin black line corresponds to a θ_p of 1° ; the thick black line corresponds to a θ_p of 10° . The magnitude of moment M_z (A), transverse force F_y (B), and axial force F_x (C) all vary over ~ 3 orders of magnitude along the vibrissa arc length.

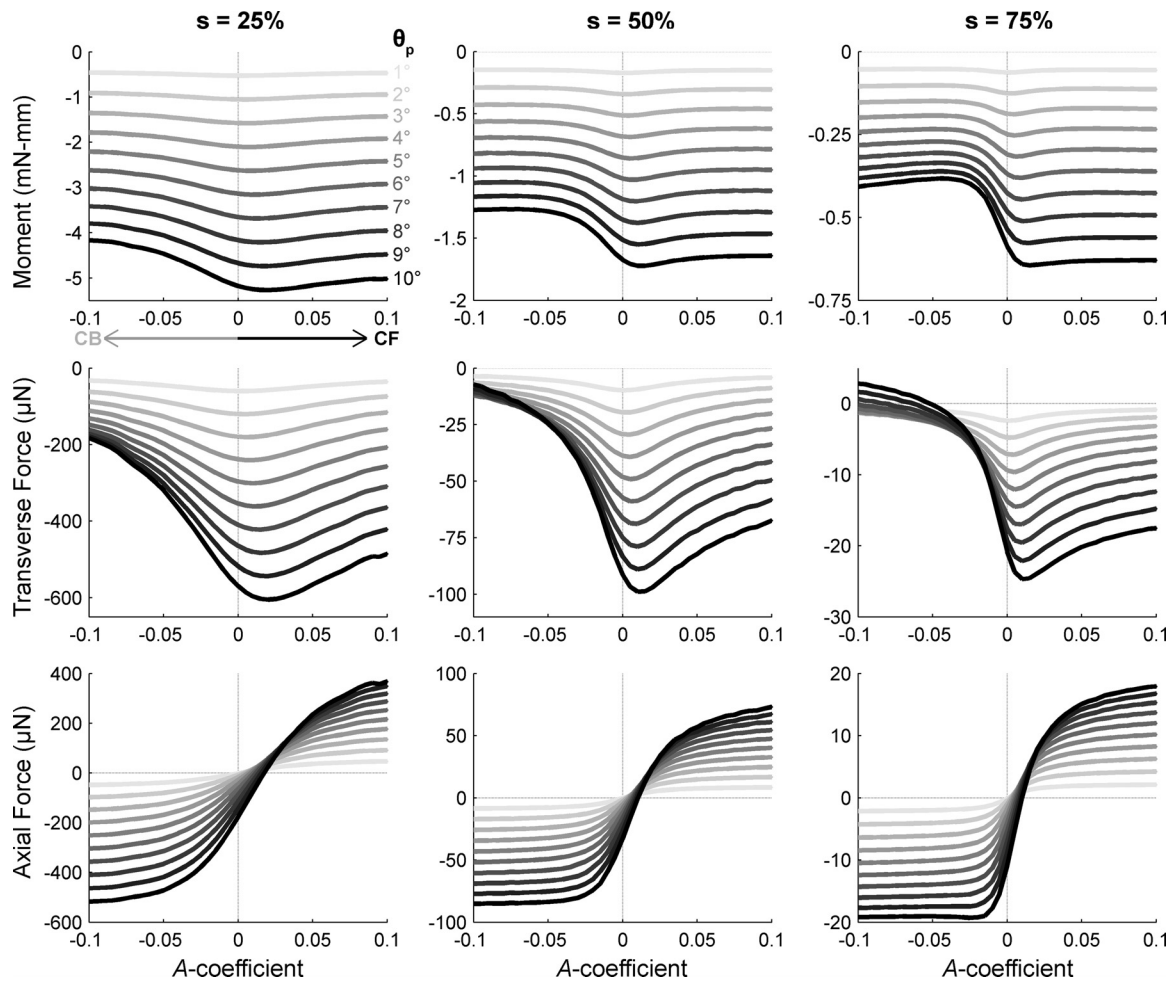


Fig. 11. Combined effect of curvature and θ_p on moments and forces at the vibrissa base. For all subplots, the pushing angle (θ_p) is indicated with color and ranges from 1° (light gray) to 10° (black) in 1° increments. Positive curvatures correspond to CF collisions; negative curvatures correspond to CB collisions. Radial object distance s is indicated as % of vibrissa arc length at top. The curves from Fig. 9 can be thought of as “slices” through these traces at for values of $A = 0$ and $A = \pm 0.0233$. Top: M_z . Middle: F_y . Bottom: F_x .

curvature at the time of collision goes from CB to CF, the sign of the axial force goes from strongly negative to strongly positive. This is because a vibrissa undergoing a CB collision compresses in on itself as θ_p increases and pushes the vibrissa into the follicle. A larger curvature (within the physiological range for vibrissae) therefore means more compression. In contrast, a CF collision will pull the vibrissa out of the follicle as θ_p increases and straighten the vibrissa.

An interesting picture of axial force emerges when we consider this result in the context of the morphology of the array. As shown in Fig. 8 and Supplemental Video S1, during natural exploratory behavior, most vibrissae in the array will tend to undergo CF collisions. The most rostral vibrissae are particularly likely to experience perfectly CF collisions. Towal et al. (2011) also showed that the more rostral vibrissae will have larger curvatures, closer to a value of $A = 0.1$. Taken together, these results suggest that the vibrissae are oriented CF on the mystacial pad in part to increase total force during distal collisions.

Experimental Results

The next sections present the results of experiments using real rat vibrissae. Experiments allow us to include friction and

other realistic nonlinearities that are not included in numerical simulations.

What are the forces and moments generated at the base of a real vibrissa as it rotates against an object? Figure 9 showed simulated forces and moments at the base of a vibrissa as it rotated against a peg placed at different radial distances from the vibrissa base. To begin to validate these simulation results, we experimentally measured the forces and moments under the same conditions. These experiments required the use of a custom-built 2D force sensor to measure the extremely small forces generated by a vibrissa (Quist and Hartmann 2008). Equal numbers of trials were performed with the CB and the CF face of the vibrissa rotating into the sensor (METHODS, Fig. 4).

Figure 12 illustrates experimental results from the C3 vibrissa that can be compared with the simulated results of Fig. 9. As found in simulation, experimental measurements show that magnitudes of moment and forces drop considerably as the object is moved closer to the vibrissa tip. CF collisions generated larger moments and transverse forces than CB collisions. CB collisions always generated negative forces that increased in magnitude with increasing θ_p .

One important difference was observed between simulation and experiment. In simulation, CF collisions generate positive

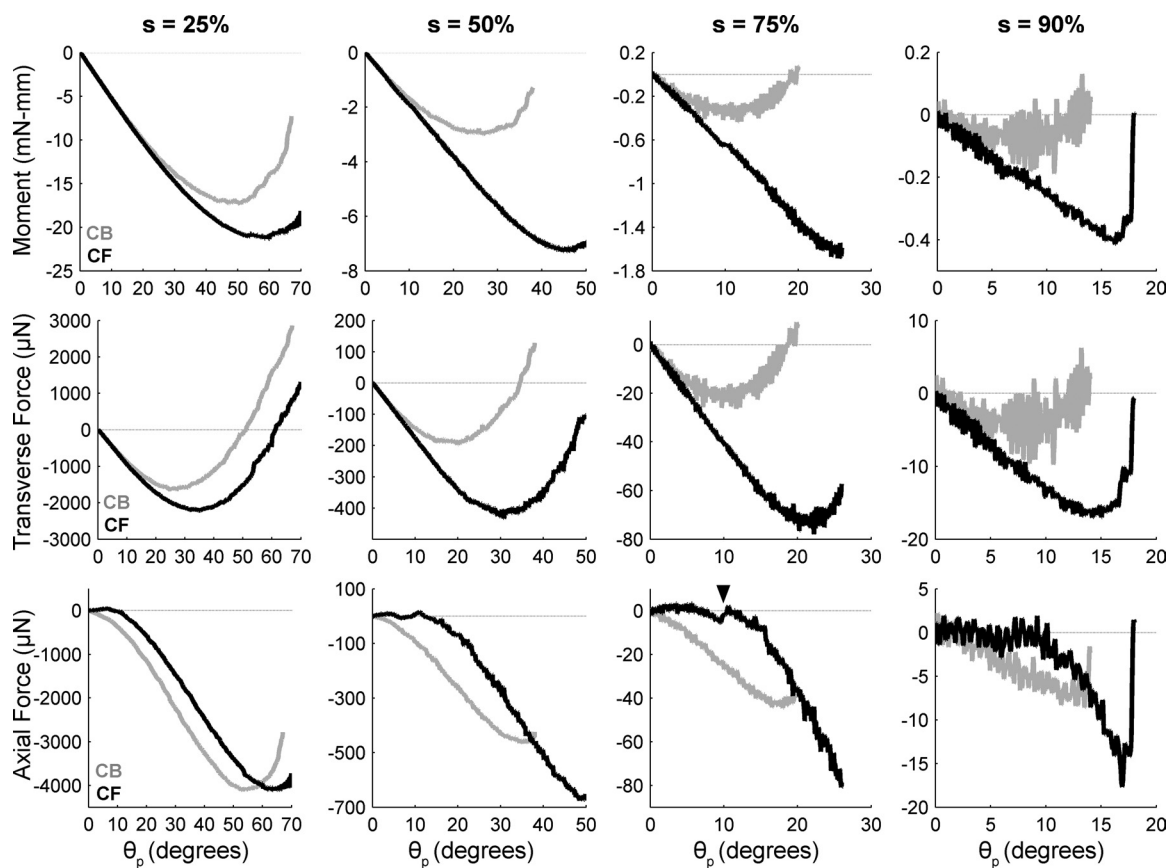


Fig. 12. Bending moment and forces measured at the base of a C3 vibrissa as it was rotated against a 2D force sensor placed at different radial distances from the vibrissa base. Angle of rotation against the sensor is the push angle, θ_p . Radial object distance s is indicated as % of vibrissa arc length at top. In all subplots, black traces represent results for a CF collision and light gray traces represent results for a CB collision. Force and moment in all plots stop when the vibrissa slipped off the sensor. Each trace represents the averaged and then filtered result of 25 individual trials. Standard deviation for all trials was $\sim 10 \mu\text{N}$ for forces and 0.3 mN-mm for moment. Top: bending moment M_z at the vibrissa base. Middle: F_y at the vibrissa base. Bottom: F_x at the vibrissa base. Arrowhead in the bottom row for $s = 75\%$ indicates a typical stick-slip event.

axial forces (Fig. 9, bottom row). In experiments, CF collisions do not generate positive axial forces. This difference is most likely due to friction. In simulation all forces act normal to the vibrissa, while in the experiment friction permits tangential forces. The presence of friction causes the vibrissa to “stick” at its initial contact point on the sensor. As the vibrissa base continues to rotate, a “slip” event ultimately occurs. This type of stick-slip event is indicated with an arrowhead for the CF axial force at $s = 75\%$ of Fig. 12.

How accurately do the simulation results model real forces and moment at the vibrissa base? We compared simulation results with measurements from real vibrissae. As described in METHODS, we left Young’s modulus as a free parameter to generate the best fit between simulation and experiment.

The top row of Fig. 13 compares the shapes of the vibrissae obtained during a simulated rotation of the vibrissa against a point object with shapes measured experimentally. Experimental data are the same as those shown in Fig. 12 (C3 vibrissa), and the simulation used geometric parameters (diameter, taper ratio, and intrinsic curvature) obtained from that same vibrissa.

For locations of vibrissa-object contact close to the vibrissa base (Fig. 13, $s = 25\%$), the shape of the vibrissa measured experimentally and the shape predicted by the model match to within the line-width of the figure. Typical errors are $\sim 4\%$ of vibrissa length. This mismatch was largely due to difficulty in

extracting the image of the vibrissa tip, which was sometimes out of the focal plane. For $s = 90\%$, simulations match experiment less well, but still to within $\sim 4\%$ error for both curvature orientations up to 10° of deflection against the object. Generally, locations of vibrissa-object contact near the base yielded better match between experiment and model, because as contacts were made closer to the vibrissa tip the vibrissa was more likely to slip out of the plane and diverge from model predictions.

The bottom row of Fig. 13 illustrates a good match between the axial and transverse forces predicted by the model and those measured experimentally, particularly for locations of vibrissa-object contact closer to the vibrissa base. As before, the elastic modulus was left as a free parameter to obtain the best match between model and experiment. A separate fit was performed for each radial distance and curvature orientation to allow for the possibility that bending stiffness depended on the direction of the deflection. A perfect match between model and experiment would lie on the diagonal of each subplot. For $s = 25\%$, CB forces fit quite well ($\sim 3\%$ maximum error for axial force, 20% maximum error for transverse force). The quality of fit was not as high for CF forces (maximum error of 13% for axial force, 25% for transverse force). Near the tip ($s = 90\%$), predictions for a CF collision were more accurate than for a CB collision. Difficulty is expected when predicting distal forces

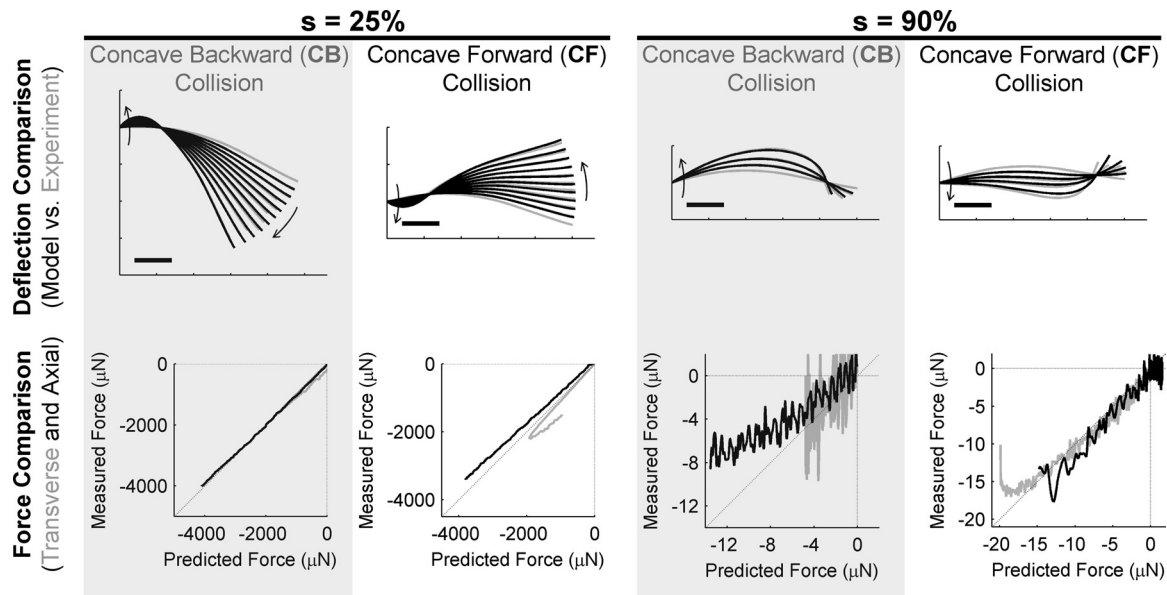


Fig. 13. Match between experiment and model. The vibrissa was rotated against a point object located either 25% or 90% out along the vibrissa length. The shape of the vibrissa and the forces generated at its base were measured experimentally, and the shape and forces were predicted from a simulation of the same rotation against the object. *Top*: the simulated shape of the vibrissa during the rotation (black) is plotted on top of the vibrissa shape measured experimentally (gray). The gray trace with no model overlay represents the undeflected shape of the vibrissa. Each trace is separated by a 5° rotation of the vibrissa. Arrows indicate the direction of the deflection. Scale bars, 5 mm. *Bottom*: differences between predicted forces and measured forces. Black, axial force; gray: transverse force.

because the vibrissa tip curves out of the plane, which violates the assumptions of the model.

How is the angle at which the vibrissa slips off an object affected by the object's radial distance and the vibrissa's curvature orientation? The angle at which the vibrissa will slip off a point object as it rotates against it is challenging to determine in simulation. This angle will depend on the 3D shape of the vibrissa, natural variability in mechanical properties, curvature of the vibrissa out of the plane near its tip, and the effects of friction.

Williams and Kramer (2010) demonstrated that the taper of the vibrissa allows it to more easily brush past an object, and that taper reduces the “maximum protraction angle” through which contact with the object can be maintained, i.e., the angle at which the vibrissa will slip off the object. For a tapered vibrissa, the maximum protraction angle becomes smaller as the contact moves closer to the tip. We confirmed this result.

In addition, we found that curvature orientation affects the angle at which the vibrissa will slip off the object. Specifically, Fig. 14 illustrates that vibrissae maintain contact with the object through a larger protraction angle for a CF collision than a CB collision. The effect is more pronounced for contacts closer to the vibrissa tip (lighter colors in Fig. 14). Thus a vibrissa will easily slip by an object at $s = 90\%$ during a CB collision but can protract up to five times further against the object during a CF collision. This makes intuitive sense because during a CF collision the vibrissa will first straighten and then continue bending before slipping past the object. In contrast, during a CB collision the vibrissa need only compress slightly. Thus the orientation of the curvature alters the physical interaction of the vibrissa with the object. CF collisions maintain longer contacts with objects.

What is the trajectory of forces that a rat will experience as it whisks against an object? The analyses above have treated the bending moment and the two components of the force as

independent variables; however, during natural whisking behavior the rat potentially has access to all of these variables (or combinations thereof) simultaneously.

The trajectories shown in Fig. 15 represent the forces the rat would experience as it whisked against an object with either the CF or the CB side of the vibrissa. These experimental data can be directly compared with the simulated results of Fig. 8.

Two important features are apparent in the force trajectories. First, for small protraction angles, the direction of the force vector depends strongly on curvature orientation. CB collisions

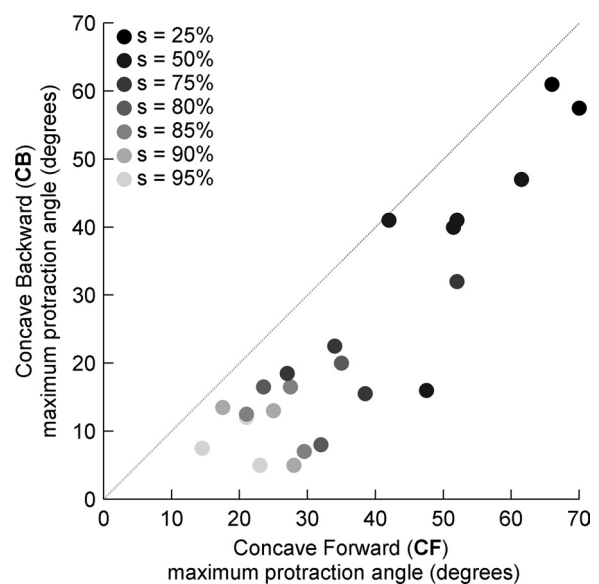


Fig. 14. The maximum angle through which the vibrissa can rotate against an object without flicking past depends on the curvature orientation. CF collisions permit the vibrissa to maintain contact with the object through a larger protraction angle than CB collisions. Marker color denotes radial distance and ranges from $s = 25\%$ (black) to $s = 95\%$ (light gray).

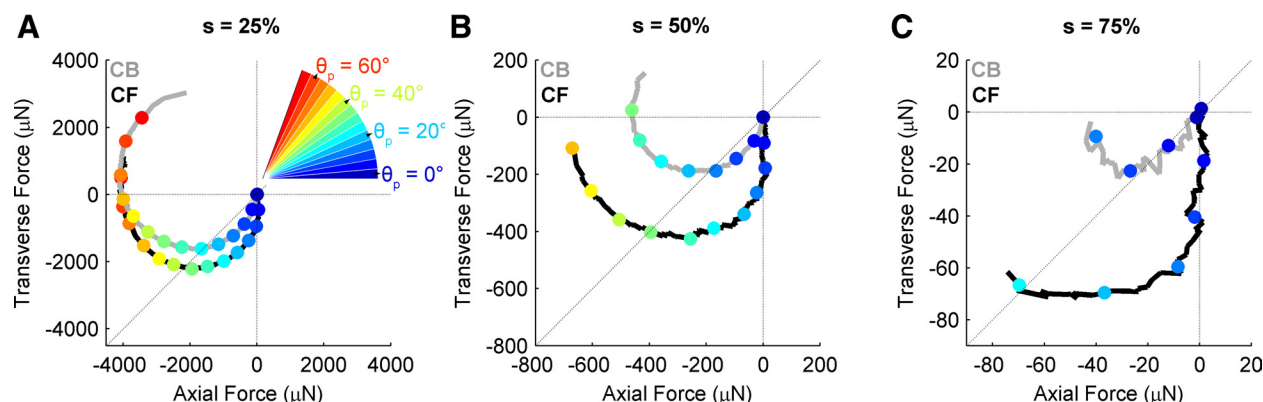


Fig. 15. Influence of curvature orientation on the trajectory of forces that will be generated at the vibrissa base. CF collisions generate larger net force vectors. For all subplots, colored circles indicate the angle through which the vibrissa has rotated against the sensor (*inset, A*). CB collision force trajectory plotted in gray; CF collision force trajectory plotted in black. *A*: force trajectory for the sensor positioned at 25% of the vibrissal arc length. *B*: force trajectory for the sensor positioned at 50% arc length. *C*: force trajectory for the sensor positioned at 75% arc length.

produce a net force vector that is balanced between axial forces and transverse forces. In contrast, CF impacts produce an initial net force vector that has small or very tiny positive axial forces. This difference is quite clear in Fig. 15C.

Second, the magnitude of the trajectory (i.e., the radius of the curves in Fig. 15) depends strongly on curvature orientation. The net force generated by CF collisions is consistently larger than the CB collision net force for a given pushing angle. For vibrissa-object contacts close to the base (Fig. 15A), the differences in net force are small. However, as the contacts move closer to the tip (Fig. 15, *B* and *C*), the difference in net force is nearly a factor of three. This ultimately means the mechanical signal will be stronger for a CF collision than a CB collision.

DISCUSSION

How does a rat sense that a vibrissa has made contact with an object? The mechanical cues that could provide this information to mechanoreceptors in the follicle are limited to forces and moments at the vibrissa base (Birdwell et al. 2007; Lottem and Azouz 2009; Solomon and Hartmann 2008, 2011).

To date, however, these mechanical cues have not been quantified. It is clear from Fig. 2A that the geometry of the sensing problem is complex and the full solution will require a 3D model. The present study, which constrains the problem to two dimensions, is one step toward our laboratory's long-term goal of completely quantifying the 3D forces and moments at the base of a vibrissa during natural whisking behavior under general conditions of object contact.

Under What Conditions Do the Results of the Present Study Apply?

The flowchart in Fig. 16 provides a guide for how to apply the present results to behavioral studies. As shown in the top box of the flowchart, the first decision point concerns how the plane of the object surface is oriented relative to the plane of rotation of the vibrissa (cf. Fig. 2). If the plane of the object surface is not oriented to minimize the vibrissa slipping out of the plane of rotation, then a 3D model will be required to account for slip of the vibrissa on the object and forces in the z -direction. The present results will not apply except for small angles of deflection.

For many behaviors, however, slip out of the plane of rotation will be minimal. This situation is particularly likely when the plane of the object surface is close to orthogonal to the plane of rotation. For example, during locomotion behaviors, the rat rhythmically dabs its head toward the ground (Grant et al. 2009; Hartmann 2001; Sellien et al. 2005; Welker 1964), so that many of the ventral vibrissae will collide directly perpendicular to the ground surface. As another example, many neurophysiological experiments place pegs or vertical walls directly in front of the rat, perpendicular to the direction of vibrissal rotation (Mehta et al. 2007; Mitchinson et al. 2007; O'Connor et al. 2010; Szwed et al. 2003). The results of the present study will hold for these behaviors and experiments.

The second decision point in the flowchart in Fig. 16 concerns whether the intrinsic vibrissa curvature lies in the plane of rotation. If it does (*case I*), then the collision will be perfectly CF or perfectly CB. The results of the present study can be directly applied, and hold for values of θ_p up to $\sim 40^\circ$. The value of A to be used can be measured directly from the intrinsic vibrissa shape at rest.

If the intrinsic vibrissa curvature does not lie in the plane of rotation (*case II*), then the collision falls somewhere between perfectly CF and perfectly CB. These collisions can be modeled by projecting the vibrissa curvature, A , into the plane of rotation to obtain the projected curvature A' , computing forces and moments, and then rotating those forces and moments back into the local vibrissa coordinate frame. The values of θ_p over which the results hold will then depend on the angle between the plane of rotation and the plane of intrinsic vibrissa curvature. If the two planes are close to parallel, then results will apply for values of θ_p as large as $\sim 40^\circ$, just as in *case I*. As the angle between the planes becomes larger, results will not hold for such large values of θ_p . The most conservative estimate is that results will hold for values of $\theta_p \leq 5^\circ$.

It is important to note that a quasi-static model such as the one described here cannot account for dynamic properties of the vibrissa, including resonance, stick-slip on an object, and the contact transients associated with a vibrissa's collision against an object. Thus the results of the present study should not be applied to a rat exploring a texture or to a vibrissa immediately after it "springs off" an object.

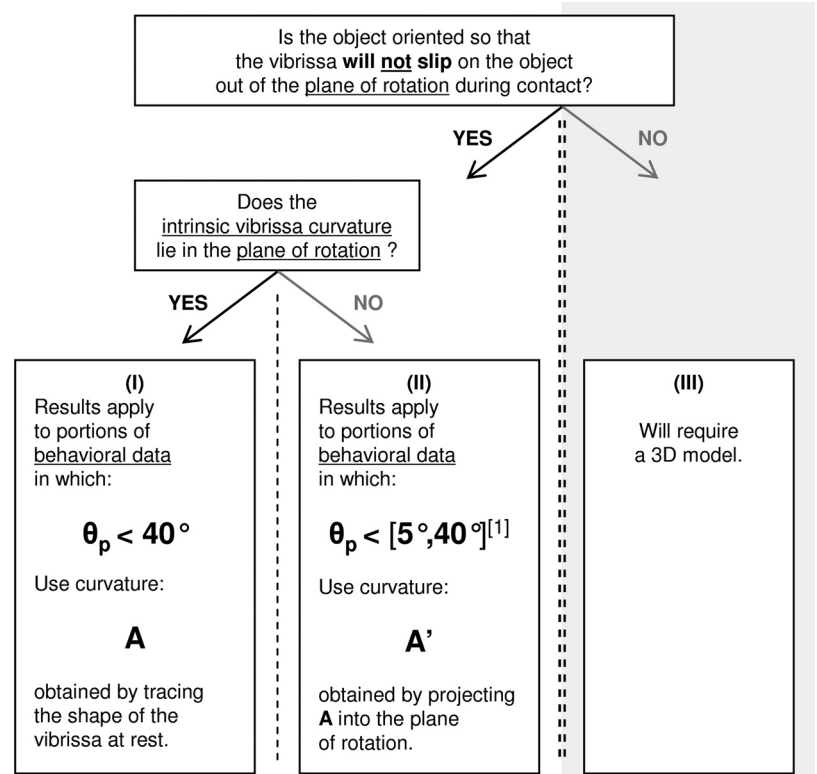


Fig. 16. Flowchart for applying the results of this study to behavioral data. ^[1]Results will apply up to θ_p of 40° , depending on the degree to which the plane of intrinsic vibrissa curvature aligns with the plane of rotation.

Most generally, then, the results of the present study will apply for collisions up to $\sim 5^\circ$ for θ_p , and in many cases may hold through much larger values of θ_p . Small ($\sim 5^\circ$) angle deflections will tend occur as the rat “dabs” or “taps” its vibrissae against an object and are characteristic of many natural exploratory behaviors, including locomotor movements along the ground or exploration of a vertical wall (Grant et al. 2009; Mitchinson et al. 2007). Importantly, even for these small angle deflections ($\theta_p < 5^\circ$), the discrepancy between the forces resulting from a CF and a CB collision can be large (see Figs. 8 and 15). Thus the orientation of the intrinsic curvature is always important, even for small push angles and regardless of how the object is placed.

Advantages of CF Vibrissa-Object Collisions

The morphology of the rat vibrissal array ensures that the majority of vibrissa-object collisions will occur with the CF face of the vibrissa facing the object (Fig. 7). CF collisions extend the protraction angle through which the vibrissa can remain in contact with an object (Fig. 14) and also generate larger net forces than CB collisions (Fig. 15). The tapered, curved geometry of the vibrissa may therefore represent a mechanical trade-off: The taper ensures rapid deflection past an object, improving the resolution with which the rat can determine the horizontal angle of vibrissa-object contact (Williams and Kramer 2010), while CF collisions ensure that forces are maximized during the collision.

Another reason CF impacts might be desirable is that they increase the probability that a vibrissa will get stuck on irregular surface features. When a vibrissa sweeps against an object with its CB face, it will become more convex to brush past the object (Fig. 8). In contrast, a vibrissa sweeping with its

CF face into an object will first straighten before becoming convex to brush past the object.

The practical consequences of this effect are highlighted in Fig. 17. A vibrissa sweeping against the object with its CB face reduces the likelihood that the tip will get stuck in any surface irregularity (Fig. 17A). In contrast, if the vibrissa sweeps with its CF face (Fig. 17B), any irregular surface features in the object will “snag” the vibrissa tip and increase the amount of bending required to continue rotating past the object. The larger bending angle translates to larger forces and moment at the base, ultimately resulting in larger signal occurring over a longer time window.

The same logic applies to a rat whisking against a surface instead of a point object, as shown in Fig. 17C. In addition, CF collisions with a wall may transmit an impulse axially along the vibrissa shaft before larger deformations begin. This impulse could permit earlier collision detection, perhaps explaining why smaller vibrissae tend to be oriented at the optimal angle for CF collisions. Axial forces transmitted by the small rostral vibrissae may be the key signal informing the rat of obstructions immediately surrounding its nose.

Neural Responses to Forces and Bending Moment

During whisking behavior, deformations of the vibrissa are transmitted to mechanoreceptors in the follicle (Ebara et al. 2002; Lottem and Azouz 2011; Mosconi et al. 1993). The response of each mechanoreceptor depends on its type (Merkel, Ruffini, etc.) as well as on its position and orientation within the follicle (Ebara et al. 2002; Mosconi et al. 1993; Rice et al. 1993). Mechanoreceptor responses are then integrated in the primary sensory neurons of the trigeminal ganglion (Vg).

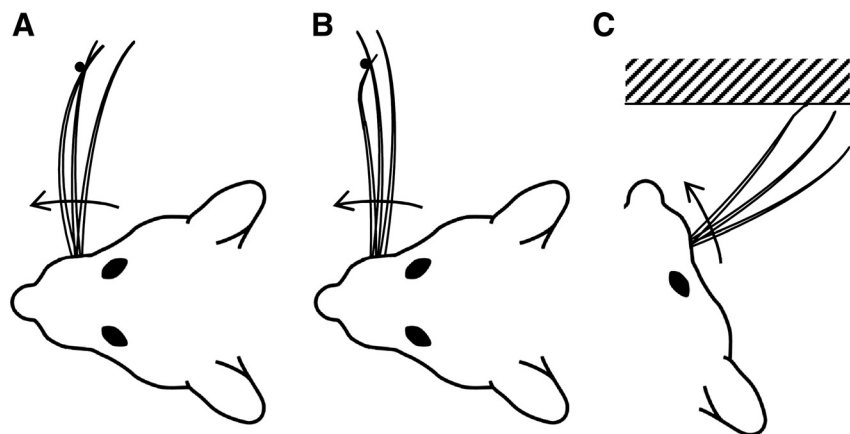


Fig. 17. Implications of the orientation of intrinsic vibrissa curvature for the behaving rat. All schematics illustrate the same vibrissa at different points in time during protraction against an object. Arrow indicates direction of protraction. *A*: CB collision of a vibrissa with a point object. As the vibrissa protracts, the vibrissa becomes more convex to slip past the object. *B*: CF collision of a vibrissa with a point object. As the vibrissa protracts, it first straightens. Next, the vibrissa tip bends backwards to permit the vibrissa to slip past the object. *C*: CF collision with a wall. As the vibrissa protracts, the tip is first to strike the surface. This may provide an initial “spike” in axial force before general deformation of the vibrissa.

In principle, the responses of Vg neurons could be predicted from the deformations of mechanoreceptors (Lottem and Azouz 2011), but these deformations are not directly observable. As an alternative, Vg responses could potentially be described in terms of the mechanics that can be observed during active behavior, namely, forces and moments at the vibrissal base. Physiological recordings will be required to determine the relationship between the complex combinations of forces and bending moments that will occur during natural behavior and Vg neural activity.

The present work makes a specific prediction for the range of forces and moments to which Vg neurons will need to respond if they are to be sensitive to contact with an object at all radial distances along the vibrissa. Figure 10 demonstrates that, for any given value of θ_p , forces and moments at the vibrissa base could vary up to three orders of magnitude, depending on where along its length the vibrissa made contact with the object. We therefore predict that Vg neurons should be responsive over this range, so as to ensure differential sensitivity at all radial distances of contact.

How Can Experimentalists Make Use of These Results When Monitoring Whisking Behavior?

In many neurophysiological studies, vibrissae are trimmed close to the base, stimulating only the short linear portion of the vibrissa that emerges directly from the mystacial pad. Trimming is performed in part to eliminate asymmetric bending moments, but these asymmetries are likely to be key variables in how the rat perceives its world. Vibrissae with different intrinsic curvatures and different curvature orientations will deflect differently when they collide with an object, in turn causing Vg neurons to respond differently.

Determining forces and moments at the base of the vibrissa may seem daunting to the experimentalist already struggling with the myriad frustrations of animal behavioral work. Although a detailed description of how to compute these mechanical variables is outside the scope of this article, we provide an outline of the basic steps. Importantly, the calculations require only measurement of vibrissa shape and/or the location of vibrissa-object contact.

The steps below assume that whisking behavior against an object is monitored with a single, high-speed overhead video camera. The assumption that forces and moment can be computed from a single camera view (2D monitoring of the vibrissa) is significant. It is likely to be accurate for small

pushing angles and for vibrissae whose intrinsic curvature is in the plane of the camera and exhibit minimum roll; these are typically the C-row vibrissae. A second camera can be used on at least some trials to validate the assumption that the vibrissa does not bend significantly out of the plane. It may also be helpful to use a depilatory cream to remove the fur around the vibrissae to permit a clear view of the vibrissa base.

First, determine the undeflected shape of the vibrissa in the video frame immediately preceding contact with the object. After the undeflected shape is obtained, there are two possible methods to compute the change in curvature at the vibrissa base.

Method 1. In each video frame after object contact, determine the deflected shape of the vibrissa. Subtracting the deflected shape from the undeflected shape yields a change in curvature at each point along the vibrissa length. This method was not used in the present study.

Method 2. In each video frame after object contact, determine 1) the location of object contact point and 2) how far the vibrissa has translated and rotated past the object. To determine the amount of translation, measure the (linear) displacement of the base point. To determine the amount of rotation, measure the change in angle of the proximal (linear) portion of the vibrissa. The undeflected vibrissa shape and contact point can then be used as input to an elastic beam model to compute curvature at the vibrissal base. This method was used to generate the simulation results in the present study.

Method 1 and *method 2* both yield estimates of change in curvature at every point along the vibrissa. Change in curvature is directly proportional to change in bending moment (Eq. 1). Quantities proportional to the forces at the vibrissal base can then be calculated based on the geometry of the vibrissa, assuming no friction. These quantities—proportional to moment and force—are likely to be sufficient for the experimentalist wanting to correlate neural activity with the animal's whisking behavior.

If it is desired to compute the actual forces and moments, then the estimates from *methods 1* and *2* must be multiplied by constants related to the stiffness of the vibrissa (Birdwell et al. 2007; Solomon and Hartmann 2006). To find the stiffness, we recommend plucking the vibrissa to measure its diameter at the base, assuming a linear taper (Williams and Kramer 2010), and approximating the elastic modulus with a value of 3.3 GPa (Quist et al. 2011).

GRANTS

This work was supported by an National Science Foundation (NSF) Graduate Research Fellowship and a National Institutes of Health (NIH) Ruth L. Kirschstein National Research Service Award (F31 NS-065630) to B. W. Quist as well as NSF awards IIS-0613568, IOS-0818414, IOS-0846088, and EFRI-0938007 to M. J. Z. Hartmann.

DISCLOSURES

No conflicts of interest, financial or otherwise, are declared by the author(s).

AUTHOR CONTRIBUTIONS

Author contributions: B.W.Q. and M.J.H. conception and design of research; B.W.Q. performed experiments; B.W.Q. and M.J.H. analyzed data; B.W.Q. and M.J.H. interpreted results of experiments; B.W.Q. prepared figures; B.W.Q. and M.J.H. drafted manuscript; B.W.Q. and M.J.H. edited and revised manuscript; B.W.Q. and M.J.H. approved final version of manuscript.

REFERENCES

- Arvidsson J, Rice FL. Central projections of primary sensory neurons innervating different parts of the vibrissae follicles and intervibrissal skin on the mystacial pad of the rat. *J Comp Neurol* 309: 1–16, 1991.
- Berg RW, Kleinfeld D. Rhythmic whisking by rat: retraction as well as protraction of the vibrissae is under active muscular control. *J Neurophysiol* 89: 104–117, 2003.
- Birdwell JA, Solomon JH, Thajchayapong M, Taylor MA, Cheely M, Towal RB, Conradt J, Hartmann MJ. Biomechanical models for radial distance determination by the rat vibrissal system. *J Neurophysiol* 98: 2439–2455, 2007.
- Brecht M, Preilowski B, Merzenich MM. Functional architecture of the mystacial vibrissae. *Behav Brain Res* 84: 81–97, 1997.
- Burn CC. What is it like to be a rat? Rat sensory perception and its implications for experimental design and rat welfare. *Appl Anim Behav Sci* 112: 1–32, 2008.
- Ebara S, Kumamoto K, Matsuura T, Mazurkiewicz JE, Rice FL. Similarities and differences in the innervation of mystacial vibrissal follicle-sinus complexes in the rat and cat: a confocal microscopic study. *J Comp Neurol* 449: 103–119, 2002.
- Grant RA, Mitchinson B, Fox CW, Prescott TJ. Active touch sensing in the rat: anticipatory and regulatory control of whisker movements during surface exploration. *J Neurophysiol* 101: 862–874, 2009.
- Hartmann M. Active sensing capabilities of the rat whisker system. *Auton Robots* 11: 249–254, 2001.
- Hartmann MJ, Johnson NJ, Towal RB, Assad C. Mechanical characteristics of rat vibrissae: resonant frequencies and damping in isolated whiskers and in the awake behaving animal. *J Neurosci* 23: 6510–6519, 2003.
- Hibbeler RC. *Mechanics of Materials*. Upper Saddle River, NJ: Pearson Prentice Hall, 2011.
- Knutsen PM, Biess A, Ahissar E. Vibrissal kinematics in 3D: tight coupling of azimuth, elevation, and torsion across different whisking modes. *Neuron* 59: 35–42, 2008.
- Lichtenstein SH, Carvell GE, Simons DJ. Responses of rat trigeminal ganglion neurons to movements of vibrissae in different directions. *Somatosens Mot Res* 7: 47–65, 1990.
- Lottem E, Azouz R. Mechanisms of tactile information transmission through whisker vibrations. *J Neurosci* 29: 11686–11697, 2009.
- Lottem E, Azouz R. A unifying framework underlying mechanotransduction in the somatosensory system. *J Neurosci* 31: 8520–8532, 2011.
- Ma PM, Woolsey TA. Cytoarchitectonic correlates of the vibrissae in the medullary trigeminal complex of the mouse. *Brain Res* 306: 374–379, 1984.
- Mehta SB, Whitmer D, Figueroa R, Williams BA, Kleinfeld D. Active spatial perception in the vibrissa scanning sensorimotor system. *PLoS Biol* 5: e15, 2007.
- Mitchinson B, Martin CJ, Grant RA, Prescott TJ. Feedback control in active sensing: rat exploratory whisking is modulated by environmental contact. *Proc Biol Sci* 274: 1035–1041, 2007.
- Mosconi TM, Rice FL, Song MJ. Sensory innervation in the inner conical body of the vibrissal follicle-sinus complex of the rat. *J Comp Neurol* 328: 232–251, 1993.
- O'Connor DH, Clack NG, Huber D, Komiyama T, Myers EW, Svoboda K. Vibrissa-based object localization in head-fixed mice. *J Neurosci* 30: 1947–1967, 2010.
- Quist BW, Faruqi RA, Hartmann MJ. Variation in Young's modulus along the length of a rat vibrissa. *J Biomech* 44: 2775–2781, 2011.
- Quist BW, Hartmann MJ. A two-dimensional force sensor in the millinewton range for measuring vibrissal contacts. *J Neurosci Methods* 172: 158–167, 2008.
- Rice FL, Kinnman E, Aldskogius H, Johansson O, Arvidsson J. The innervation of the mystacial pad of the rat as revealed by PGP 9.5 immunofluorescence. *J Comp Neurol* 337: 366–385, 1993.
- Sellien H, Eshenroder DS, Ebner FF. Comparison of bilateral whisker movement in freely exploring and head-fixed adult rats. *Somatosens Mot Res* 22: 97–114, 2005.
- Solomon JH, Hartmann MJ. Artificial whiskers suitable for array implementation: accounting for lateral slip and surface friction. *IEEE Trans Robot Automat* 24: 1157–1167, 2008.
- Solomon JH, Hartmann MJ. Biomechanics: robotic whiskers used to sense features. *Nature* 443: 525, 2006.
- Solomon JH, Hartmann MJ. Extracting object contours with the sweep of a robotic whisker using torque information. *Int J Robotics Res* 29: 1233–1245, 2010.
- Solomon JH, Hartmann MJ. Radial distance determination in the rat vibrissal system and the effects of Weber's law. *Philos Trans R Soc Lond B Biol Sci* 366: 3049–3057, 2011.
- Stuttgen MC, Kullmann S, Schwarz C. Responses of rat trigeminal ganglion neurons to longitudinal whisker stimulation. *J Neurophysiol* 100: 1879–1884, 2008.
- Szwed M, Bagdasarian K, Ahissar E. Encoding of vibrissal active touch. *Neuron* 40: 621–630, 2003.
- Towal RB, Quist BW, Gopal V, Solomon JH, Hartmann MJ. The morphology of the rat vibrissal array: a model for quantifying spatiotemporal patterns of whisker-object contact. *PLoS Comput Biol* 7: e1001120, 2011.
- Vanderloos H. Barreloids in mouse somatosensory thalamus. *Neurosci Lett* 2: 1–6, 1976.
- Welker WI. Analysis of sniffing of the albino rat. *Behaviour* 22: 223–224, 1964.
- Williams CM, Kramer EM. The advantages of a tapered whisker. *PLoS One* 5: e8806, 2010.
- Woolsey TA, Welker C, Schwartz RH. Comparative anatomical studies of the SmL face cortex with special reference to the occurrence of "barrels" in layer IV. *J Comp Neurol* 164: 79–94, 1975.